Published in final edited form as:

J Am Chem Soc. 2022 July 06; 144(26): 11608–11619. doi:10.1021/jacs.2c01809.

Selective Isotope Labeling and LC-Photo-CIDNP Enable NMR Spectroscopy at Low-Nanomolar Concentration

Hanming Yang[a], **Clayton A. Mickles**[a], **Valeria Guzman-Luna**[a], **Kenji Sugisaki**[b,c], **Siyu Li**[a], **Clayton M. Thompson**[a], **Hung H. Dang**[a], **Silvia Cavagnero**[a]

[a]Department of Chemistry, University of Wisconsin - Madison, 1101 University Ave., Madison, Wisconsin, 53706, USA.

[b]Department of Chemistry, Graduate School of Science, Osaka Metropolitan University, 3-3-138 Sugimoto, Sumiyoshi-ku, Osaka, 558-8585, Japan.

[c]JST PRESTO, 4-1-8 Honcho, Kawaguchi, Saitama 332-0012, Japan.

Abstract

NMR spectroscopy is a powerful tool to investigate molecular structure and dynamics. The poor sensitivity of this technique, however, limits its ability to tackle questions requiring dilute samples. Low-concentration photo-chemically induced dynamic nuclear polarization (LC-photo-CIDNP) is an optically-enhanced NMR technology capable of addressing the above challenge by increasing the detection limit of aromatic amino acids in solution up to 1,000-fold, either in isolation or within proteins. Here, we show that the absence of NMR-active nuclei close to a magnetically active site of interest (e.g., the structurally diagnostic H^{α}-C^{α} pair of amino acids) is expected to significantly increase LC-photo-CIDNP hyperpolarization. Then, we exploit the spin-diluted tryptophan isotopolog Trp-α-^{13}C-β,β,2,4,5,6,7-d_7 and take advantage of the above prediction to experimentally achieve a ca 4-fold enhancement in NMR sensitivity over regular LC-photo-CIDNP. This advance enables the rapid (within seconds) detection of 20 nM concentrations or the molecule of interest, corresponding to a remarkable 3 ng detection limit. Finally, the above Trp isotopolog is amenable to incorporation within proteins and is readily detectable at 1 μM concentration in complex cell-like media, including *E. coli* cell-free extracts.

Correspondence should be addressed to S.C. (cavagnero@chem.wisc.edu, Phone: 608-262-5430).

Other Authors

Hanming Yang – Department of Chemistry, University of Wisconsin - Madison, 1101 University Ave., Madison, Wisconsin, 53706, USA; Present Address: Affinity Research Chemicals, 406 Meco Dr., Wilmington, Deleware, 19804, USA.

Clayton A. Mickles – Department of Chemistry, University of Wisconsin - Madison, 1101 University Ave., Madison, Wisconsin, 53706, USA.

Valeria Guzman-Luna – Department of Chemistry, University of Wisconsin - Madison, 1101 University Ave., Madison, Wisconsin, 53706, USA.

Kenji Sugisaki – Department of Chemistry and Molecular Materials Science, Osaka City University, 3-3-138 Sugimoto, Sumiyoshi-ku, Osaka, 558-8585, Japan.

Siyu Li – Department of Chemistry, University of Wisconsin - Madison, 1101 University Ave., Madison, Wisconsin, 53706, USA.

Clayton M. Thompson – Department of Chemistry, University of Wisconsin - Madison, 1101 University Ave., Madison, Wisconsin, 53706, USA; Present Address: PPD Inc, 8551 Research Way, Middleton, Wisconsin, 53652-4664, USA.

Hung H. Dang – Department of Chemistry, University of Wisconsin - Madison, 1101 University Ave., Madison, Wisconsin, 53706, USA.

ASSOCIATED CONTENT

The Supporting Information is available free of charge at [URL TBD].

Description of theoretical predictions on photo-CIDNP polarization, additional experimental details on NMR transvers relaxation measurements, description of assessment of LED-on and LED-off effects used to generate Table 1, experimental section.

Graphical Abstract

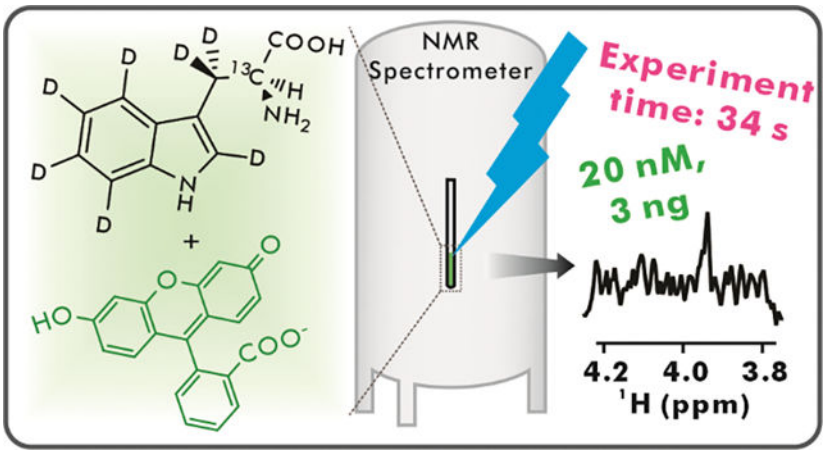

Keywords

Hyperpolarization; photo-CIDNP; NMR; isotope labeling

Introduction

Nuclear magnetic resonance (NMR) spectroscopy is a non-invasive technique capable of yielding invaluable information on molecular structure and dynamics at atomic resolution. On the other hand, NMR is intrinsically insensitive due to small differences in population between nuclear spin eigenstates, even at the highest commercially available magnetic field of 28.2 T (1, 2). Although low sensitivity can be compensated by increased sample concentration, this is often not a feasible option due to limited solubility, small amounts of material and high aggregation propensities. The above challenges are particularly severe in the case of biological samples in aqueous media. Numerous hyperpolarization methods were developed to increase the sensitivity of liquid-state NMR by altering nuclear spin populations at thermal equilibrium. Major developments comprise Overhauser dynamic nuclear polarization (ODNP) (3–5), dissolution dynamic nuclear polarization (DDNP) (6–8), and parahydrogen-induced polarization (PHIP) (9–15), including signal amplification by reversible exchange (SABRE) (16–33).

On the other hand, a few challenges have hampered the wide applicability of the above hyperpolarization technologies, to date. These include expensive instrumentation, harsh sample conditions (e.g., high/low temperatures, freeze-thaw cycles), long hyperpolarization times, applicability to a limited number of molecules of interest, safety considerations, inability to perform *in situ* hyperpolarization, requirement of high sample concentration (50 μM or more) and unfeasible data collection in physiologically relevant environments.

Earlier identification of chemically induced dynamic nuclear polarization (CIDNP) (34, 35) in organic reactions led to the development of a photochemically enhanced NMR approach known as photo-CIDNP. While originally employed to assess solvent exposure (36), this technique has more recently been employed to significantly increase NMR sensitivity in

solution at high applied field (37–43). Photo-CIDNP is devoid of most of the drawbacks of other approaches listed in the previous paragraph. This technique requires aromatic moieties and benefits from an O_2-free environment.

Photo-CIDNP exploits spin-selective processes between a molecule of interest and a photosensitizer dye. The phenomenon proceeds via a radical pair mechanism, as shown in Figure 1A. Photo-CIDNP can be employed for NMR sensitivity enhancement purposes (44) and, when combined with heteronuclear correlation spectroscopy, it enables highly sensitive detection of hyperpolarized ^{13}C and ^{15}N (38, 39, 45). More recently, trace amounts of commercially available glucose oxidase (GO) and catalase (CAT) were employed to remove dissolved molecular oxygen, thus preventing excited-state dye quenching and further increasing NMR sensitivity (37). The use of fluorescein (Fig. 1B) as photosensitizer, in place of flavin mononucleotide (FMN), led to extension of this technique to low sample concentration (low- to sub-μM) (40). The use of photosensitizers characterized by a long triplet-state lifetime (e.g., 20 ms for fluorescein (40, 46)) gave rise to a branch of photo-CIDNP known as low-concentration photo-CIDNP (LC-photo-CIDNP). Replacement of costly and hard-to-maintain high-power laser with LEDs (Fig. 1C) with no sensitivity losses led to enhanced ease of access, portability and safety (42).

LC-photo-CIDNP performs optimally at low-to-sub μM sample concentration (40, 41), and it provides fast (0.2 s) *in situ* nuclear hyperpolarization. The latter features enable long-term signal-averaging and multi-dimensional NMR of extremely dilute samples. This technology leads to enhanced signal-to-noise ratio (S/N) of tryptophan (Trp) and tyrosine (Tyr), either as free amino acids or within polypeptides and proteins (38, 41–43). Remarkably, high LC-photo-CIDNP enhancements are observed for C^{α} nuclei of aromatic amino acids, likely due to their high hyperfine coupling constants (38, 47), enabling the efficient detection of H^{α}-C^{α} pairs. The C^{α} chemical shifts are particularly useful because they are diagnostic of backbone secondary structure in proteins (48). To take advantage of proton's higher sensitivity, ^{13}C-to-^{1}H polarization transfer via reverse INEPT is typically employed (38). In addition, 2D data collection is carried out to preserve information on $^{13}C^{\alpha}$ chemical shifts (38, 41). The recently developed ^{13}C RASPRINT pulse sequence is optimized for ultra-fast data collection in aqueous solvent (42).This sequence exploits minimal recycle delays, given that most nuclear-spin polarization is generated during the optical irradiation time, thus abrogating the need for lengthy inter-scan intervals (42). The ^{13}C RASPRINT sequence is particularly useful for the ultra-rapid detection of H^{α}-C^{α} pairs at low sample concentration, down to ca. 500 nM (42). More recent studies showed that LC-photo-CIDNP hyperpolarization can be further enhanced in the presence of low-μM concentrations of reductive radical quenchers including ascorbic acid, a.k.a. vitamin C, leading to detection of 200 nM aromatic amino acids (43). Despite the above advances, it is highly desirable to render liquid-state NMR spectroscopy even more sensitive so that it approaches detection limits of other leading techniques, e.g., fluorescence and mass spectrometry.

In this work, we provide theoretical and experimental evidence illustrating that nearby NMR-active nuclei (e.g., ^{1}H's, ^{13}C and ^{15}N) significantly decrease the extent of observable ^{13}C LC-photo-CIDNP polarization. Upon replacement of these nuclei with either NMR-inactive (^{12}C) or low-gyromagnetic-ratio (^{2}H) nuclei by selective isotope labeling, we were

able to achieve an unprecedented improvement in NMR detection level in solution, down to 20 nM Trp, in only a few seconds. In addition, we showed that the above isotopolog-assisted optically enhanced technology is also effective in complex cell-like media, enabling the analysis of aromatic amino acids in physiologically relevant milieu at atomic resolution and extremely high sensitivity.

RESULTS AND DISCUSSION

Theoretical predictions on the dependence of LC-photo-CIDNP-hyperpolarization on isotope substitution patterns and g-factor values.

LC-photo-CIDNP polarization depends on the g-factor of the radical form of the reduced photosensitizer dye. Fluorescein is typically employed as a dye. The g-factor of its reduced radical form in solution, however, is not known. Note that different protonation states of fluorescein in solution are expected to affect g-factor values. We carried out density functional theory (DFT) calculations to estimate the pK_a and g-factor of the fluorescein dye radical at 25 °C and pH 7.0. Water solvation effects were taken into account via the integral equation formalism polarizable continuum model (IEFPCM). Predicted g-factor values were determined for the fully protonated state of the $Fl^{\bullet}$ dye radical and for seven variably deprotonated states, as listed in Figure 2A. The pK_a values of the three titratable protons were employed to determine the population of each of the eight variably protonated species listed in Figure 2A via the Henderson-Hasselbalch equation. The resulting individual populations and corresponding g-factors were employed to predict the overall weighted-average g-factor of the fluorescein dye radical at 25 °C and pH 7.0. This g-factor value was mostly contributed by $Fl^{\bullet -}$, and was found to be 2.003077.

The known g-factor of $Trp^{\bullet +}$ (47) and the weighted-average g-factor of the fluorescein dye radical, determined as described in the previous paragraph, were used as input for computational predictions of LC-photo-CIDNP polarization as a function of g-factor of the dye radical. We followed known theoretical and practical guidelines (49–51), with some modifications, as detailed below.

For freely-diffusing radical pairs, the population difference between any two nuclear-spin configurations 1 and 2 of the geminate-recombination product is

$$p_1 - p_2 = p\left(\sqrt{|\omega_{TS1}|\tau_d} - \sqrt{|\omega_{TS2}|\tau_d}\right) \ , \qquad [1]$$

where p_1, p_2 are the populations with nuclear-spin configuration 1 and 2, respectively; p is a normalization factor (see Supplementary Information), ω_{TS1} and ω_{TS2} are the triplet-singlet mixing frequencies of the nuclear-spin configurations, and τ_d is the average time the radical-pair components remain closely associated (beyond orbital-overlap distances) before long-term dissociation. The triplet-singlet mixing frequency of each of any possible nuclear-spin configurations is

$$\omega_{TS} = \frac{1}{2}\left[\Delta g \mu_B B_0 + \sum_i m_i A_i - \sum_j m_j A_j\right] \ , \qquad [2]$$

where the *i* and *j* subscripts denote individual nuclei of the dye and molecule of interest, respectively. In addition, Δg is the difference between the g-factors of the radical-pair components (i.e., the dye and molecule of interest), μ_B denotes the Bohr's magneton B_0 is the applied magnetic field, and m and A are the magnetic nuclear-spin quantum number and hyperfine coupling constant, respectively.

For different isotope labeling schemes of the molecule of interest, corresponding to different isotopologs, the third term of equation [2] is expected to vary depending on specific A_j values. Therefore, we reasoned that different isotopic substitutions ought to give rise to variable populations of geminate-pair products, resulting into different levels of photo-CIDNP hyperpolarization (52). Hence we proceeded to explore how the g-factor of dye radicals is expected to affect the theoretically achievable geminate-pair recombination products, in the case of different Trp isotopologs. We focused on three representative labeling schemes of the molecule of interest: namely, *(i)* uniformly ^{13}C-labeled Trp (Trp-U-^{13}C), *(ii)* a hypothetical Trp isotopolog bearing a ^{13}C-^{1}H pair at the α carbon (C^{α}) and extensive deuteration at non-exchangeable sites (Trp-α-^{13}C-β,β,2,4,5,6,7-d_7, Fig. 3A), and, finally, *(iii)* a reference Trp isotopolog enriched in ^{13}C at the C^{α} and bearing natural-abundance nuclides at all other sites (Trp-α-^{13}C, Fig. 3B). Importantly, all of the above isotopologs have a ^{13}C at the α position, honoring the fact that the LC-photo-CIDNP hyperpolarization approach is particularly effective at enhancing the $^{13}C^{\alpha}$ of the Trp and Tyr amino acids, either alone or within proteins (41). Additional details about the computations, including assessment of overall probabilities of geminate recombination, proportional to nuclear-spin polarization at the Trp α carbon, are provided in the Supplementary Information.

The simulation results for the above three Trp isotopologs are shown in Figure 2B. Even at optimal values of g-factor of the dye radical, the two compounds bearing no deuteration are predicted to afford only limited sensitivity enhancement. On the other hand, the Trp-α-^{13}C-β,β,2,4,5,6,7-d_7 deuterated isotopolog (solid circles in the plot of Fig. 2B) is expected to undergo drastic polarization enhancements that significantly vary in magnitude depending on the g-factor of the dye radical. These enhancements extend up to nearly 14.5% for dyes that bear an optimal g-factor value.

Under typical LC-photo-CIDNP conditions, fluorescein is employed as photosensitizer (41). As detailed elsewhere (40), this dye bears a conveniently long triplet-state lifetime that persists across the infrequent collisions between dye and molecule of interest, at moderate sample concentrations (low μM and lower). Therefore, despite its sub-optimal g-factor value in the plot of Figure 2B, fluorescein is the current photosensitizer of choice in LC-photo-CIDNP experiments. When fluorescein is employed as a photosensitizer at room temperature and 25 °C, the predicted probability of geminate recombination (proportional to nuclear-spin hyperpolarization (52)) of uniformly ^{13}C-labeled Trp (Trp-U-^{13}C) is the lowest (ca. 5%). On the other hand, Trp-α-^{13}C is predicted to experience a 4.4% more geminate-recombination than Trp-U-^{13}C. More strikingly, the selectively labeled isotopolog Trp-α-^{13}C-β,β,2,4,5,6,7-d_7, which includes extensive deuteration at C^{β} and aromatic carbon sites, is predicted to experience 28.2% more geminate recombination than Trp-U-^{13}C.

Trp analogs bearing variable isotopic substitution patterns were prepared and characterized.

Encouraged by the computational predictions of Figure 2B, we proceeded to prepare some relevant isotopologs and experimentally test their performance in terms of achievable LC-photo-CIDNP hyperpolarization.

Previous selective labeling schemes were based on supplementing bacterial growth media with [4-^{13}C]-δ-aminolevulinic acid (53) or with different singly labeled ^{13}C-glucose isotopologs (54). These methods, however, suffer from low isotope-incorporation yields and are not easily customizable to the desired labeling patterns. Here, we employed an alternative recently developed enzyme-cascade approach (55) to readily achieve high levels of isotope enrichment starting from affordable and readily available precursors. This approach is particularly convenient due to its modular nature (55). For instance, it enables the facile synthesis of a wide variety of desired isotopologs by simply changing the labeling pattern of the starting materials (i.e., glycine and indole) and solvent (water).

The synthetic schemes of Figure 3A and 3B detail the route that led to the generation of Trp-α-^{13}C-β,β,2,4,5,6,7-d$_7$ and Trp-α-^{13}C with 44.7% and 31.8% yield, respectively. Given that the amounts of purified products were more than adequate for our purposes, no further optimization was performed. The identity of purified Trp-α-^{13}C-β,β,2,4,5,6,7-d$_7$ and Trp-α-^{13}C was confirmed by ESI MS and ^{1}H NMR. The pulse-acquire ^{1}H NMR spectra of the two isotopologs are shown in Figure 3C and 3D and confirm the presence of the expected ^{13}C-^{1}H scalar coupling. The latter disappears upon ^{13}C decoupling. In addition, no ^{1}H aromatic resonances are observed for Trp-α-^{13}C-β,β,2,4,5,6,7-d$_7$, consistent with expectations.

The Trp-α-^{13}C-β,β,2,4,5,6,7-d$_7$ isotopolog leads to large LC-photo-CIDNP sensitivity enhancements.

The two Trp isotopologs described in the previous section and the commercially available uniformly labeled Trp-U-^{13}C,^{15}N were initially analyzed under dark (i.e., LED-off) conditions. The ^{13}C RASPRINT pulse sequence (42) was employed, except that the typically short recycle delays (50 ms) (42) were replaced by long ones (5 s) to allow for nearly complete longitudinal relaxation. This pulse sequence enables the detection of ^{13}C-bound protons and is routinely employed in LC-photo-CIDNP (42).

Figure 4A, which focuses on H$^{\alpha}$ protons under dark conditions, shows that the selectively labeled Trp-α-^{13}C and Trp-α-^{13}C-β,β,2,4,5,6,7-d$_7$ isotopologs display a larger S/N than uniformly labeled Trp (Trp-U-^{13}C,^{15}N). While Figure 4A provides a useful qualitative assessment, the different sample concentrations prevent quantitative comparisons. A more quantitative analysis of NMR behavior under dark conditions is provided in Figure 4B. The plot in this figure examines both intensities at the resonance maximum and areas, and normalizes the data so that they are independent of sample concentration. Here we note that, relative to Trp-U-^{13}C,^{15}N, the Trp-α-^{13}C isotopolog displays 20% increases in resonance area and intensity at the maximum. Conversely, Trp-α-^{13}C-β,β,2,4,5,6,7-d$_7$ displays a 42% increase in area and an even more dramatic 192% increase in intensity at the maximum. The

latter enhancement results from narrower ^{1}H linewidths, as confirmed by T_2 measurements (Supplementary Information). In summary, perhaps not surprisingly, detection of Trp H^{α} resonances under dark conditions is rendered more facile by the extensive deuteration of the Trp-α-^{13}C-β,β,2,4,5,6,7-d_7 isotopolog. It is worth noting that H^{α} resonances are important in biology because they are diagnostic of structure, especially when analyzed in the context of protein backbone.

Next, we performed 1D LC-photo-CIDNP experiments on all three Trp isotopologs under light (i.e., LED-on) conditions. Data were collected at very low sample concentration (1μM). The NMR spectra under light conditions, shown in Figure 4C, display considerable increases in S/N upon going from Trp-U-^{13}C,^{15}N to Trp-α-^{13}C to Trp-α-^{13}C-β,β,2,4,5,6,7-d_7. Remarkably, the latter isotopolog displays a ca. 4-fold increase in S/N relative to the already intense signal of uniformly labeled Trp (Trp-U-^{13}C,^{15}N). More quantitative studies, displayed in Figure 4D, show that Trp-α-^{13}C displays a 70% increase in resonance area and intensity relative to Trp-U-^{13}C,^{15}N, while Trp-α-^{13}C-β,β,2,4,5,6,7-d_7 features a 120% increase in area and a 300% increase in resonance intensity.

At this juncture, it is important to consider a few simple items. First, NMR sensitivity (1, 56) is defined as S/N divided by the square root of experiment time t, i.e., $\frac{S}{N\sqrt{t}}$. Second, the NMR S/N ratio depends on the amplitude of both the resonance of interest and the noise. Third, all data were collected with identical acquisition and processing parameters. Taking all of the above considerations into account, the results of Figure 4C and 4D clearly show that the Trp-α-^{13}C-β,β,2,4,5,6,7-d_7 isotopolog displays a remarkable 4-fold increase in sensitivity relative to uniformly labeled Trp (Trp-U-^{13}C,^{15}N). Note that all experiments under light conditions must bear equivalent noise values. This result is even more significant if one notices that (a) all the Figure 4C spectra acquired under dark conditions display no detectable signal, and (b) all the Figure 4 light and dark spectra included only 32 scans. In conclusion, the overall sensitivity of the ^{13}C RASPRINT experiment for the Trp-α-13C-β,β,2,4,5,6,7-d_7 isotopolog must be very high. More details on specific enhancements factors and polarization values are provided in a later section.

The Trp-α-^{13}C-β,β,2,4,5,6,7-d_7 isotopolog enables optically-enhanced NMR at low nanomolar concentration.

Encouraged by the results described in the previous sections, we further explored the LC-photo-CIDNP detection limit of the Trp-α-^{13}C-β,β,2,4,5,6,7-d_7 isotopolog. Towards this end, we took a few deliberate simple steps. First, to optimize detection of the target isotopolog, we modified the ^{13}C RASPRINT pulse sequence by removing its constant-time evolution. Note that the absence of ^{13}Cs at the β and carbonyl positions ($^{13}C^{\beta}$ and ^{13}C') of the Trp-α-^{13}C-β,β,2,4,5,6,7-d_7 isotopolog renders constant-time evolution unnecessary, due to lack of ^{13}C-^{13}C J couplings (57). Second, we converted all the on-resonance selective pulses into hard pulses and removed the ^{13}C' off-resonance pulse. These modifications are justified by the fact that the Trp-α-^{13}C-β,β,2,4,5,6,7-d_7 isotopolog only bears one ^{13}C and lacks ^{13}C-^{13}C J couplings. Therefore, there is no need for $^{13}C^{\alpha}$ selective excitation or for selective C' pulses to refocus $^{13}C^{\alpha}$–^{13}C' J couplings.

Importantly, all the above modifications are beneficial because they lead to shorter experiment times and reduce signal losses arising from pulse imperfections and transverse relaxation during the pulse scheme. The resulting pulse sequence, displayed in Figure 5A, was denoted as ^{13}C isotopolog-optimized RASPRINT or ^{13}C iso-RASPRINT.

Then, we tested the LC-photo-CIDNP behavior of extremely dilute (50 and 20 nM) Trp-α-^{13}C-β,β,2,4,5,6,7-d$_7$ upon data collection with the ^{13}C iso-RASPRINT pulse sequence. The results (two outmost-left spectra in Fig. 5B) show that the 50 nM sample yields a detectable resonance of moderate intensity after 64 scans (Fig. 5B). On the other hand, the 20 nM sample displayed no observable signal (data not shown). Given that reductive radical quenchers including ascorbic acid, also known as vitamin C (VC) is known to protect LC-photo-CIDNP molecules of interest from photodamage (43), potentially extending detection limit, we prepared an additional set of samples containing a small concentration of VC (2 μM). The results, shown in the four righthandside panels of Figure 5B, prove that in the presence of the VC reductive radical quencher even 20 nM Trp-α-^{13}C-β,β,2,4,5,6,7-d$_7$ can be readily detectable, within only 64 scans. This is a remarkably small concentration, corresponding to an extremely favorable detection limit of 3 ng.

Quantitative assessment of LC-photo-CIDNP enhancements and polarization values.

To more quantitatively evaluate the extent of polarization enhancement generated via LC-photo-CIDNP for each of the isotopologs analyzed in this work, we compared resonance areas under dark and light conditions according to the relation below

$$\varepsilon = \frac{Area_{light}}{Area_{dark}} \frac{[Trp]_{dark}}{[Trp]_{light}} \quad , \qquad [3]$$

where ε is the polarization enhancement factor, defined as the ratio between nuclear spin polarization under light and dark conditions. Note that we acquired the dark (LED-off) spectra at much higher concentrations (ca. 100 μM) than the LED-on experiments, and then adjusted for concentration differences according to equation [3]. In addition, we employed long (5 s) recycle delays to ensure nearly complete relaxation between scans. We collected the same number of scans under dark and light conditions. Clearly, if the shorter delays employed in the light experiments had been employed for data collection under dark conditions, the apparent polarization enhancement factors would have been much larger. We refrained from doing this so that we could provide the highest possible reference S/N values under dark conditions.

From percent polarization enhancements ε and from thermal-equilibrium percent polarization $P_{\%,te}$, assessed from the Boltzmann distribution in the presence of a 600 MHz applied field (1), we also determined the percent polarization $P_{\%}$ according to

$$P_{\%} = \varepsilon P_{\%,te} \quad . \qquad [4]$$

The resulting ε and $P_{\%}$ values of all three isotopologs examined in this work are shown in Figure 6.

The enhancement factor and percent polarization of the two best isotopologs are discussed next. As shown in Figure 6, the ε and $P_{\%}$ values of Trp-α-^{13}C are 410 ± 2 and 0.496 ± 0.003%, respectively. The Trp-α-^{13}C-β,β,2,4,5,6,7-d_7 displays the highest values; namely ε and $P_{\%}$ of 470 ± 13 and 0.568 ± 0.016%. The Trp-α-^{13}C and Trp-α-^{13}C-β,β,2,4,5,6,7-d_7 isotopologs performed considerably better than uniformly labeled Trp (Trp-U-^{13}C,^{15}N), with increases of 38% and 57%, respectively.

The observed sensitivity enhancements arise from both LED-on and LED-off effects.

The data of Figure 4B, collected under dark (LED-off) conditions, show that selective ^{13}C labeling as well as introduction of deuteration at C^{β} and across the aromatic ring induces some sensitivity enhancement even in the absence of optical irradiation. Therefore, some non-photo-CIDNP-related factors must contribute to the overall observed effects.

We were able to identify two specific dark-state contributions. First, there was an increase in $^{1}H^{\alpha}$ T_2 arising from either the removal of some nearby NMR-active nuclei and(or) from their replacement with low-gyromagnetic-ratio (low-γ) nuclei due to selective labeling. The results of $^{1}H^{\alpha}$ T_2 measurements are presented in the Supplementary Information. Clearly, this effect accounts for the sharper resonances, and longer $^{1}H^{\alpha}$ T_2 displayed by the Trp-α-^{13}C-β,β,2,4,5,6,7-d_7 isotopolog even under dark conditions. Second, the elimination of many ^{13}C-^{13}C, multi-bond ^{1}H-^{13}C and ^{1}H-^{1}H J couplings arising from selective labeling prevents loss of coherence via J coupling during the pulse sequence. This effect was quantified upon comparing the area/concentration ratios for the $^{1}H^{\alpha}$ resonance of each isotopolog in LC-photo-CIDNP measurements carried out under dark conditions.

In addition, there were also contributions due to LC-photo-CIDNP hyperpolarization effects under light (LED-on) conditions expected from the theoretical arguments discussed in the previous sections. The contributions arising from all three factors (linewidth reduction, J-coupling effects and LC-photo-CIDNP hyperpolarization) were quantified as described in the Supplementary Text and Supplementary Figure S4. The results are summarized in Table 1 for each of the isotopologs examined in this work. For easier-evaluation purposes, the data were normalized relative to Trp-U-^{13}C,^{15}N. The product of all three separately-assessed contributions agrees well with the overall enhancement factor in sensitivity. Overall, it is intriguing to note that the sensitivity enhancements described in this work were achieved by a combination of “dark and light effects”.

LC-photo-CIDNP is effective in complex biologically relevant media.

In addition to the simple environments discussed so far, including only few purified components, LC-photo-CIDNP can also be applied to samples within extremely complex biological *milieux*. To demonstrate this capability in the case of the LC-photo-CIDNP technology presented here, we prepared an *E. coli* S30 bacterial cell extract according to known procedures (58). This extract includes most *E. coli* soluble proteins. The composition of the corresponding NMR sample is schematically illustrated in Figure 7A and the procedure followed to generate the cell extract is outlined in Figure 7B. Importantly, this complex biological sample included 1 μM Trp-α-^{13}C-β,β,2,4,5,6,7-d_7. Figure 7C illustrates the fact that no signal was observable for this extremely dilute Trp isotopolog under dark

conditions. In contrast, 1 μM Trp-α-^{13}C-β,β,2,4,5,6,7-d_7 became readily detected after only 8 scans under light conditions. Remarkably, due to the nearly absent recycle delay of ^{13}C iso-RASPRINT under light conditions, the entire data collection, including the hyperpolarization time, only took a total of ca. 4 s (excluding the time for the 4 dummy scans, i.e., 2 additional seconds).

Comparisons with other hyperpolarization approaches in liquids.

As a comparison, two representative examples from other leading nuclear-spin hyperpolarization approaches will be listed next. The well-known dissolution DNP (dDNP) technology enabled detection of 20 μM protein samples (59). This technology has also been used in the context of protein-ligand interactions (6, 60–65). In addition, Kouřil *et al.* (66) recently showed that 32% ^{13}C polarization was rendered possible by bullet-DNP, an interesting variation of dDNP employing small sample-dilution factors during the dissolution process. In both the above studies, considerably higher sample concentrations were required than in the present work. Moreover, unlike LC-photo-CIDNP, the dDNP approach requires a freeze-thaw process that is not always desirable in the case of biomolecules.

Very recent studies showed that parahydrogen-induced polarization (PHIP), especially via the SABRE approach, can be employed for the detection of amino acids in solution (18, 67, 68). While this methodology is promising, identification of suitable amino-acid precursors for SABRE remains difficult, and extension of this technique to proteins has not been feasible.

CONCLUSIONS AND OUTLOOK

In this study we introduce a combination of LC-photo-CIDNP and selective isotope labeling to enable the NMR detection of low-nM biomolecular concentrations by liquid-state NMR. The use of selective isotope labeling enables an additional ca. 4-fold increase in sensitivity relative to a uniformly isotopically enriched reference molecule (Trp-U-^{13}C,^{15}N). This gain in sensitivity was crucial to access the low-nanomolar (20 nM) concentration range, providing a remarkable detection limit of only 3 ng in a few seconds. To the best of our knowledge, this is the lowest concentration achieved by high-resolution biomolecular NMR in liquids to date. Our methodology works well even in extremely complex physiologically relevant environments, including an *E. coli* S30 cell extract. The capability to assess Trp levels (69–71), metabolism and transport in biological media is important because of the emerging role of this amino acid and its metabolites in health and disease (72–78).

Importantly, the LC-photo-CIDNP technology, including the advances presented here, is also readily amenable to extensions to Trp-containing macromolecules. For instance, LC-photo-CIDNP of polypeptides and proteins has already been established (38, 41, 43), and it yields comparable enhancements to free Trp. Further, given that Trp analogs can be routinely incorporated into proteins via auxotroph strains (79), one can envisage that the same strains can also be employed to incorporate Trp isotopologs like Trp-α-^{13}C-β,β,2,4,5,6,7-d_7 into proteins. Ultrasensitive detection of H^{α}-C^{α} pairs in proteins is highly desirable because it provides access to site-specific information on backbone secondary structure (48).

Further, the ^{13}C iso-RASPRINT pulse sequence can readily be run in 2D mode to resolve overlapping resonances within mixtures of aromatic amino acids or in the context of large biomolecules.

In all, the advances described in this work pave the way to a variety of biomolecular NMR applications requiring high sensitivity and fast data collection. It will be exciting to follow the forthcoming progress of this technology in the years to come.

Supplementary Material

Refer to Web version on PubMed Central for supplementary material.

ACKNOWLEDGMENTS

We thank Alexandra Yurkovskaya and Andrew Buller for insightful discussions, and Greg Sabat for assistance with mass spectrometry. We are grateful to Charles G. Fry, Heike Hofstetter and Cathy Clewett for technical assistance with NMR. Some of this research was performed using the computer resources and assistance of the UW-Madison Center for High Throughput Computing (CHTC) in the Department of Computer Sciences (80, 81). The CHTC is supported by UW-Madison, the Advanced Computing Initiative, the Wisconsin Alumni Research Foundation, the Wisconsin Institutes for Discovery, and the National Science Foundation, and is an active member of the OSG Consortium, which is supported by the National Science Foundation and the U.S. Department of Energy's Office of Science.

FUNDING SOURCES

This work was funded by the National Institutes of Health (grants R01GM125995 and S10OD012245), from the National Science Foundation (grant MCB 2124672) and from the University of Wisconsin-Madison (Bridge Funds from the College of Letters & Science).

REFERENCES

1. Lee JH, Okuno Y, Cavagnero S, Sensitivity enhancement in solution NMR: emerging ideas and new frontiers. J. Magn. Reson. 241, 18–31 (2014). [PubMed: 24656077]
2. Ardenkjaer-Larsen JH et al. , Facing and overcoming sensitivity challenges in biomolecular NMR spectroscopy. Angew. Chem. Int. Ed. 54, 9162–9185 (2015).
3. Schops P, Spindler PE, Prisner TF, Multi-frequency pulsed Overhauser DNP at 1.2 Tesla. Zeit. Phys. Chem. Intl. J. Res. Phys. Chem. Chem. Phys. 231, 561–573 (2017).
4. Denysenkov VP, Prisner TF, Liquid-state Overhauser DNP at high magnetic fields. Emagres 8, 41–54 (2019).
5. Bennati M, Orlando T, Overhauser DNP in liquids on 13C nuclei. Emagres 8, 11–18 (2019).
6. Kim Y, Hilty C, "Applications of Dissolution-DNP for NMR Screening" in Biological Nmr, Pt B, Wand AJ, Ed. (2019), vol. 615, pp. 501–526.
7. Kagawa A et al. , High-field NMR with dissolution triplet-DNP. J. Magn. Reson. 309, 106623 (2019). [PubMed: 31669795]
8. Jahnig F et al. , A spin-thermodynamic approach to characterize spin dynamics in TEMPO-based samples for dissolution DNP at 7 T field. J. Magn. Reson. 303, 91–104 (2019). [PubMed: 31030064]
9. Bowers CR, Weitekamp DP, Transformation of symmetrization order to nuclear-spin magnetization by chemical reaction and nuclear magnetic resonance. Phys. Rev. Lett. 57, 2645–2648 (1986). [PubMed: 10033824]
10. Bowers CR, Weitekamp DP, Parahydrogen and synthesis allow dramatically enhanced nuclear alignment. J. Am. Chem. Soc. 109, 5541–5542 (1987).

11. Carson PJ, Bowers CR, Weitekamp DP, The PASADENA effect at a solid surface: High-sensitivity nuclear magnetic resonance of hydrogen chemisorption. J. Am. Chem. Soc. 123, 11821–11822 (2001). [PubMed: 11716749]
12. Pravica MG, Weitekamp DP, Net NMR alignment by adiabatic transport of parahydrogen addition products to high magnetic field. Chem. Phys. Lett. 145, 255–258 (1988).
13. Wang WY et al. , Pairwise stereoselective hydrogenation of propyne on supported Pd-Ag catalysts investigated by parahydrogen-induced polarization. J. Phys. Chem. C 125, 17144–17154 (2021).
14. Salnikov OG et al. , Heterogeneous 1H and 13C parahydrogen-Induced polarization of acetate and pyruvate esters. ChemPhysChem 22, 1389–1396 (2021). [PubMed: 33929077]
15. Pokochueva EV, Burueva DB, Salnikov OG, Koptyug IV, Heterogeneous catalysis and parahydrogen-induced polarization. ChemPhysChem 22, 1421–1440 (2021). [PubMed: 33969590]
16. Adams RW et al. , Reversible interactions with para-hydrogen enhance NMR sensitivity by polarization transfer. Science 323, 1708–1711 (2009). [PubMed: 19325111]
17. Duckett SB, Mewis RE, Application of Parahydrogen Induced Polarization Techniques in NMR Spectroscopy and Imaging. Acc. Chem. Res. 45, 1247–1257 (2012). [PubMed: 22452702]
18. Pravdivtsev AN, Buntkowsky G, Duckett SB, Koptyug IV, Hovener JB, Parahydrogen-induced polarization of amino acids. Angew. Chem. 60, 23496–23507 (2021). [PubMed: 33635601]
19. Taylor DA, Natrajan LS, Nilsson M, Adams RW, SABRE-enhanced real-time pure shift NMR spectroscopy. Magn. Reson. Chem. 59, 1244–1252 (2021). [PubMed: 34405451]
20. Spiridonov KA et al. , Phosphite-containing iridium polarization transfer catalysts for NMR signal amplification by reversible exchange. Mendeleev Commun. 31, 475–477 (2021).
21. Kiryutin AS, Yurkovskaya AV, Petrov PA, Ivanov KL, Simultaneous ^{15}N polarization of several biocompatible substrates in ethanol-water mixtures by signal amplification by reversible exchange (SABRE) method. Magn. Reson. Chem. 59, 1216–1224 (2021). [PubMed: 34085303]
22. Barskiy DA et al. , The Feasibility of Formation and Kinetics of NMR Signal Amplification by Reversible Exchange (SABRE) at High Magnetic Field (9.4 T). J. Am. Chem. Soc. 136, 3322–3325 (2014). [PubMed: 24528143]
23. Barskiy DA et al. , In Situ and Ex Situ Low-Field NMR Spectroscopy and MRI Endowed by SABRE Hyperpolarization. ChemPhysChem 15, 4100–4107 (2014). [PubMed: 25367202]
24. Feng BB, Coffey AM, Colon RD, Chekmenev EY, Waddell KW, A pulsed injection parahydrogen generator and techniques for quantifying enrichment. J. Magn. Reson. 214, 258–262 (2012). [PubMed: 22188975]
25. Shchepin RV et al. , N-15 Hyperpolarization of Imidazole-N-15(2) for Magnetic Resonance pH Sensing via SABRE-SHEATH. Acs Sensors 1, 640–644 (2016). [PubMed: 27379344]
26. Shchepin RV et al. , Hyperpolarization of “Neat” Liquids by NMR Signal Amplification by Reversible Exchange. Journal of Physical Chemistry Letters 6, 1961–1967 (2015). [PubMed: 26029349]
27. Shi F, Coffey AM, Waddell KW, Chekmenev EY, Goodson BM, Heterogeneous Solution NMR Signal Amplification by Reversible Exchange. Angewandte Chemie-International Edition 53, 7495–7498 (2014). [PubMed: 24889730]
28. Shi F, Coffey AM, Waddell KW, Chekmenev EY, Goodson BM, Nanoscale Catalysts for NMR Signal Enhancement by Reversible Exchange. J. Phys. Chem. C 119, 7525–7533 (2015).
29. Shi F et al. , Aqueous NMR Signal Enhancement by Reversible Exchange in a Single Step Using Water-Soluble Catalysts. J. Phys. Chem. C 120, 12149–12156 (2016).
30. Theis T, Truong M, Coffey AM, Chekmenev EY, Warren WS, LIGHT-SABRE enables efficient in-magnet catalytic hyperpolarization. J. Magn. Reson. 248, 23–26 (2014). [PubMed: 25299767]
31. Theis T et al. , Microtesla SABRE Enables 10% Nitrogen-15 Nuclear Spin Polarization. J. Am. Chem. Soc. 137, 1404–1407 (2015). [PubMed: 25583142]
32. Truong ML et al. , Irreversible Catalyst Activation Enables Hyperpolarization and Water Solubility for NMR Signal Amplification by Reversible Exchange. J. Phys. Chem. B 118, 13882–13889 (2014). [PubMed: 25372972]
33. Truong ML et al. , N-15 Hyperpolarization by Reversible Exchange Using SABRE-SHEATH. J. Phys. Chem. C 119, 8786–8797 (2015).

34. Bargon J, Fischer H, Johnsen U, Kernresonanz-emissionslinien während rascher radikalreaktionen. Zeitschrift für Naturforschung A 22, 1551–1555 (1967).
35. Ward HR, Lawler RG, Nuclear magnetic resonance emission and enhanced absorption in rapid organometallic reactions. J. Am. Chem. Soc. 89, 5518–5519 (1967).
36. Kaptein R, Dijkstra K, Nicolay K, Laser photo-CIDNP as a surface probe for proteins in solution. Nature 274, 293–294 (1978). [PubMed: 683312]
37. Lee JH, Cavagnero S, A novel tri-enzyme system in combination with laser-driven NMR enables efficient nuclear polarization of biomolecules in solution. J. Phys. Chem. B 117, 6069–6081 (2013). [PubMed: 23560683]
38. Lee JH, Sekhar A, Cavagnero S, ^{1}H-Detected ^{13}C photo-CIDNP as a sensitivity enhancement tool in solution NMR. J. Am. Chem. Soc. 133, 8062–8065 (2011). [PubMed: 21548581]
39. Lyon CE, Jones JA, Redfield C, Dobson CM, Hore PJ, Two-dimensional ^{15}N-^{1}H photo-CIDNP as a surface probe of native and partially structured proteins. J. Am. Chem. Soc. 121, 6505–6506 (1999).
40. Okuno Y, Cavagnero S, Fluorescein: a photo-CIDNP sensitizer enabling hypersensitive NMR data collection in liquids at low micromolar concentration. J. Phys. Chem. B 120, 715–723 (2016). [PubMed: 26744790]
41. Okuno Y et al. , Laser- and cryogenic probe-assisted NMR enables hypersensitive analysis of biomolecules at submicromolar concentration. Proc. Natl. Acad. Sci. USA 116, 11602–11611 (2019). [PubMed: 31142651]
42. Yang H, Hofstetter H, Cavagnero S, Fast-pulsing LED-enhanced NMR: A convenient and inexpensive approach to increase NMR sensitivity. J. Chem. Phys. 151, 245102 (2019). [PubMed: 31893873]
43. Yang H, Mecha MF, Goebel CP, Cavagnero S, Enhanced nuclear-spin hyperpolarization of amino acids and proteins via reductive radical quenchers. J. Magn. Reson. 324, 106912 (2021). [PubMed: 33524671]
44. Kaptein R, Dijkstra K, Müller F, Van Schagen CG, Visser AJWG, 360-MHz laser-induced phot-CIDNP in photoreaction of flavins. J. Magn. Reson. 31, 171–176 (1978).
45. Hore PJ, Broadhurst RW, Photo-CIDNP of biopolymers. Prog. Nucl. Magn. Reson. Spectrosc. 25, 345–402 (1993).
46. Lindqvist L, A flash photolysis study of fluorescein. Arkiv for Kemi 16, 79–138 (1961).
47. Kiryutin AS, Morozova OB, Kuhn LT, Yurkovskaya AV, Hore PJ, ^{1}H and ^{13}C Hyperfine coupling constants of the tryptophanyl cation radical in aqueous solution from microsecond time-resolved CIDNP. J. Phys. Chem. B 111, 11221–11227 (2007). [PubMed: 17764168]
48. Spera S, Bax A, Empirical correlation between protein backbone conformation and C^{α}. and C^{β}. ^{13}C nuclear magnetic resonance chemical shifts. J. Am. Chem. Soc. 113, 5490–5492 (1991).
49. Adrian FJ, Singlet-triplet splitting in diffusing radical pairs and magnitude of chemically induced electron-spin polarization. J. Chem. Phys. 57, 5107 (1972).
50. Ivanov KL, Pravdivtsev AN, Yurkovskaya AV, Vieth HM, Kaptein R, The role of level anti-crossings in nuclear spin hyperpolarization. Prog. Nucl. Magn. Reson. Spectrosc. 81, 1–36 (2014). [PubMed: 25142733]
51. Lyon CE, Lopez JJ, Cho BM, Hore PJ, Low field CIDNP of amino acids and proteins: characterization of transient radicals and NMR sensitivity enhancement. Mol. Phys. 100, 1261–1269 (2002).
52. Okuno Y, Cavagnero S, Photochemically induced dynamic nuclear polarization: basic principles and applications. eMagRes 6, 283–313 (2017).
53. Janssen GJ et al. , Observation of the solid-state photo-CIDNP effect in entire cells of cyanobacteria synechocystis. Photosynth. Res. 104, 275–282 (2010). [PubMed: 20094793]
54. Eisenreich W et al. , Strategy for enhancement of ^{13}C-photo-CIDNP NMR spectra by exploiting fractional ^{13}C-labeling of tryptophan. J. Phys. Chem. B 119, 13934–13943 (2015). [PubMed: 26244593]
55. Thompson CM, McDonald AD, Yang H, Cavagnero S, Buller AR, Modular control of L-tryptophan isotopic substitution via an efficient biosynthetic cascade. Org. Biomol. Chem. 18, 4189–4192 (2020). [PubMed: 32452506]

56. Ernst RR, Bodenhausen G, Wokaun A, Principles of nuclear magnetic resonance in one and two dimensions (Oxford University Press, New York, 1989).
57. Cavanagh J, Fairbrother W, Palmer AI, R. M, NJ S, Protein NMR Spectroscopy Principles and Practice (Elsevier Academic Press, ed. 2nd, 2007).
58. Bakke CK, Jungbauer LM, Cavagnero S, In vitro expression and characterization of native apomyoglobin under low molecular crowding conditions. Prot. Eng. Expr. Purif. 45, 381–392 (2006).
59. Ragavan M, Iconaru LI, Park C-G, Kriwacki RW, Hilty C, Real-time analysis of folding upon binding of a disordered protein by using dissolution DNP NMR spectroscopy. Angew. Chem. 56, 7070–7073 (2017). [PubMed: 28508552]
60. Kim J, Mandal R, Hilty C, Characterization of Membrane Protein-Lipid Interactions in Unfolded OmpX with Enhanced Time Resolution by Hyperpolarized NMR. Chembiochem 21, 2861–2867 (2020). [PubMed: 32419259]
61. Kim Y, Liu MX, Hilty C, Parallelized Ligand Screening Using Dissolution Dynamic Nuclear Polarization. Anal. Chem. 88, 11178–11183 (2016). [PubMed: 27723298]
62. Kim Y, Liu MX, Hilty C, Determination of binding affinities using hyperpolarized NMR with simultaneous 4-channel detection. J. Magn. Reson. 295, 80–86 (2018). [PubMed: 30144688]
63. Kim Y, Wang YY, Chen HY, Hilty C, “In-Vitro Dissolution Dynamic Nuclear Polarization for Sensitivity Enhancement of NMR with Biological Molecules” in Protein NMR: Methods and Protocols, Ghose R, Ed. (2018), vol. 1688, pp. 155–168.
64. Liu MX, Kim Y, Hilty C, Characterization of Chemical Exchange Using Relaxation Dispersion of Hyperpolarized Nuclear Spins. Anal. Chem. 89, 9154–9158 (2017). [PubMed: 28714674]
65. Wang YY, Kim J, Hilty C, Determination of protein-ligand binding modes using fast multi-dimensional NMR with hyperpolarization. Chemical Science 11, 5935–5943 (2020). [PubMed: 32874513]
66. Kouřil K, Kouřilová H, Bartram S, Levitt MH, Meier B, Scalable dissolution-dynamic nuclear polarization with rapid transfer of a polarized solid. Nature Comm. 10, 1733 (2019).
67. Kaltschnee L et al. , Hyperpolarization of amino acids in water utilizing parahydrogen on a rhodium nanocatalyst. Chem. Eur. J. 25, 11031–11035 (2019). [PubMed: 31347750]
68. Sellies L, Aspers R, Feiters MC, Rutjes F, Tessari M, Parahydrogen hyperpolarization allows direct NMR detection of alpha-amino acids in complex (bio)mixtures. Angew. Chem. 60, 26954–26959 (2021). [PubMed: 34534406]
69. Kositz C et al. , High serum tryptophan concentration in pollinosis patients is associated with unresponsiveness to pollen extract therapy. Int. Arch. All. Immun. 147, 35–40 (2008).
70. Menta R et al. , Tryptophan concentration is the main mediator of the capacity of adipose mesenchymal stromal cells to inhibit T-lymphocyte proliferation in vitro. Cytother. 16, 1679–1691 (2014).
71. Weinlich G, Murr C, Richardsen L, Winkler C, Fuchs D, Decreased serum tryptophan concentration predicts poor prognosis in malignant melanoma patients. Dermatol. 214, 8–14 (2007).
72. Agus A, Planchais J, Sokol H, Gut Microbiota Regulation of Tryptophan Metabolism in Health and Disease. Cell Host & Microbe 23, 716–724 (2018). [PubMed: 29902437]
73. Bosi A, Banfi D, Bistoletti M, Giaroni C, Baj A, Tryptophan Metabolites Along the Microbiota-Gut-Brain Axis: An Interkingdom Communication System Influencing the Gut in Health and Disease. Int. J. Tryp. Res. 13, 1–25 (2020).
74. Gao K, Mu CL, Farzi A, Zhu WY, Tryptophan Metabolism: A Link Between the Gut Microbiota and Brain. Adv. Nutr. 11, 709–723 (2020). [PubMed: 31825083]
75. Gostner JM et al. , Tryptophan Metabolism and Related Pathways in Psychoneuroimmunology: The Impact of Nutrition and Lifestyle. Neuropsychobiol. 79, 89–99 (2020).
76. Kokturk O, Kanbay A, “Tryptophan Metabolism and Sleep” in Tryptophan Metabolism: Implications for Biological Processes, Health and Disease, Engin A, Engin AB, Eds. (2015), pp. 239–252.
77. Konopelski P, Ufnal M, Indoles - Gut Bacteria Metabolites of Tryptophan with Pharmacotherapeutic Potential. Curr. Drug Met. 19, 883–890 (2018).

78. Roth W, Zadeh K, Vekariya R, Ge Y, Mohamadzadeh M, Tryptophan Metabolism and Gut-Brain Homeostasis. International Journal of Molecular Sciences 22, 1877–2013 (2021). [PubMed: 33668642]

79. Broos J, “Biosynthetic incorporation of tryptophan analogs in proteins” in Fluorescence spectroscopy and microscopy - methods and protocols, Engelborghs Y, Visser AJWG, Eds. (Humana Press, New York, 2014), chap. 15, pp. 359–370.

80. Pordes R et al. (2007) The open science grid. in 3rd Annual Scientific Discovery through Advanced Computing Conference (SciDAC 2007) (Boston, MA).

81. Sfiligoi I et al. , The Pilot Way to Grid Resources Using glideinWMS. WRI World Congress on Computer Science and Information Engineering 2, 428–432 (2009).

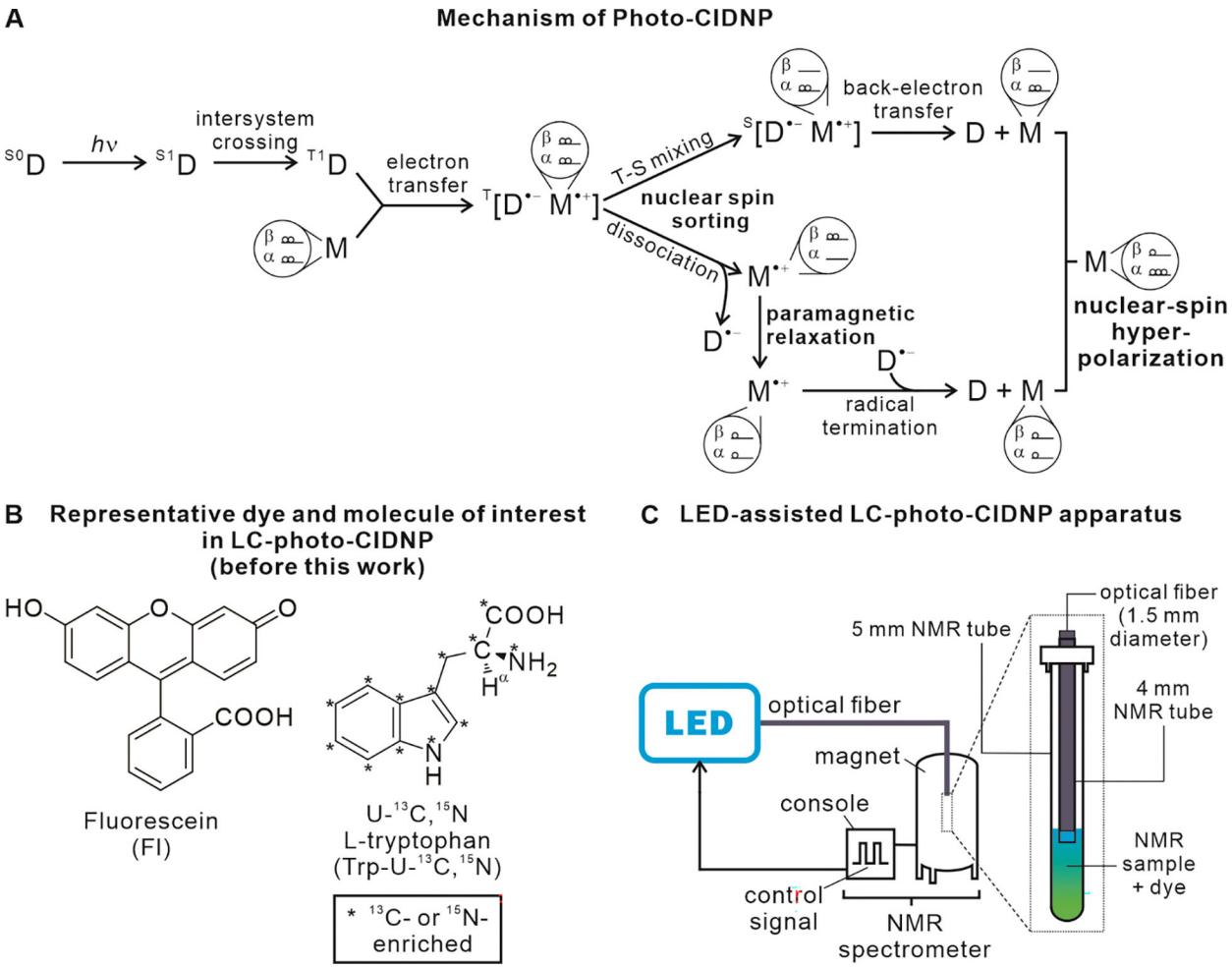

Figure 1. Basic aspects of low-concentration photo-chemically induced dynamic nuclear polarization (LC-photo-CIDNP).

A. Schematic illustration of the radical-pair mechanism of photo-CIDNP in liquids. D and M denote the dye and molecule of interest, respectively. S_0, S_1 and T_1 refer to the ground singlet, 1st excited singlet and 1st excited electronic triplet states, respectively. The T-S acronym denotes triplet-singlet mixing. The frequency of T-S mixing of the $^{T}[D^{\bullet-}M^{\bullet+}]$ radical pair depends on the nuclear spin states of the molecule of interest $M^{\bullet+}$, due to hyperfine coupling between unpaired electron and nuclear spins. Therefore, depending on the value of nuclear spin states, molecules can either undergo fast or slow T-S mixing. The population with nuclear spin states undergoing slow T-S mixing experiences radical-pair dissociation followed by paramagnetic relaxation, resulting in thermal nuclear-spin polarization. Conversely, the population with nuclear spin states experiencing fast T-S mixing undergoes T-S mixing followed by fast back electron transfer. Importantly, this population experiences nuclear-spin hyperpolarization. In practice, one detects the sum of the two populations, in a photo-CIDNP experiment. B. Structure of a typical small molecule of interest and photosensitizer dye employed in LC-photo-CIDNP. C. Scheme illustrating typical LC-photo-CDINP instrumentation.

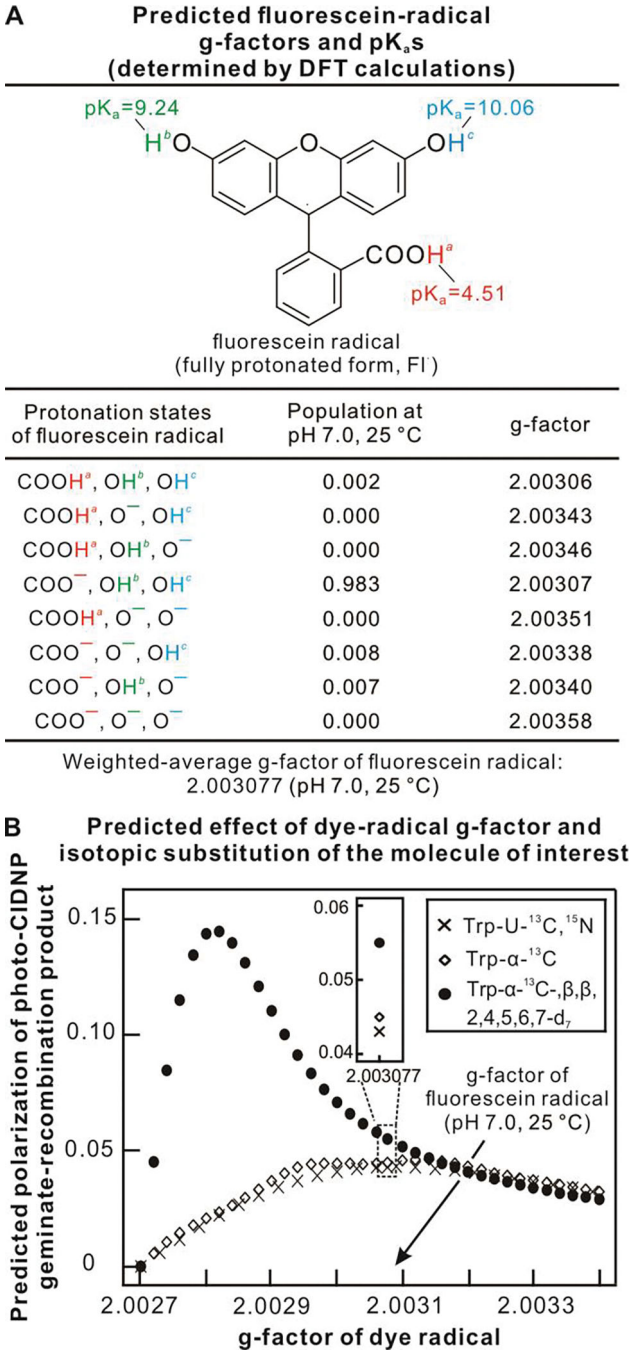

Figure 2. Computational predictions.

A. Predicted pK_a and isotropic g-factor values for fluorescein radicals of different protonation states. B. Predicted photo-CIDNP polarization of three Trp isotopologs as a function of dye g-factor. Simulations were performed using g-factor of $Trp^{\bullet}$ = 2.0027, and hyperfine coupling constant of Trp and fluorescein radicals from literature sources (see details in Suppl. Inf.).

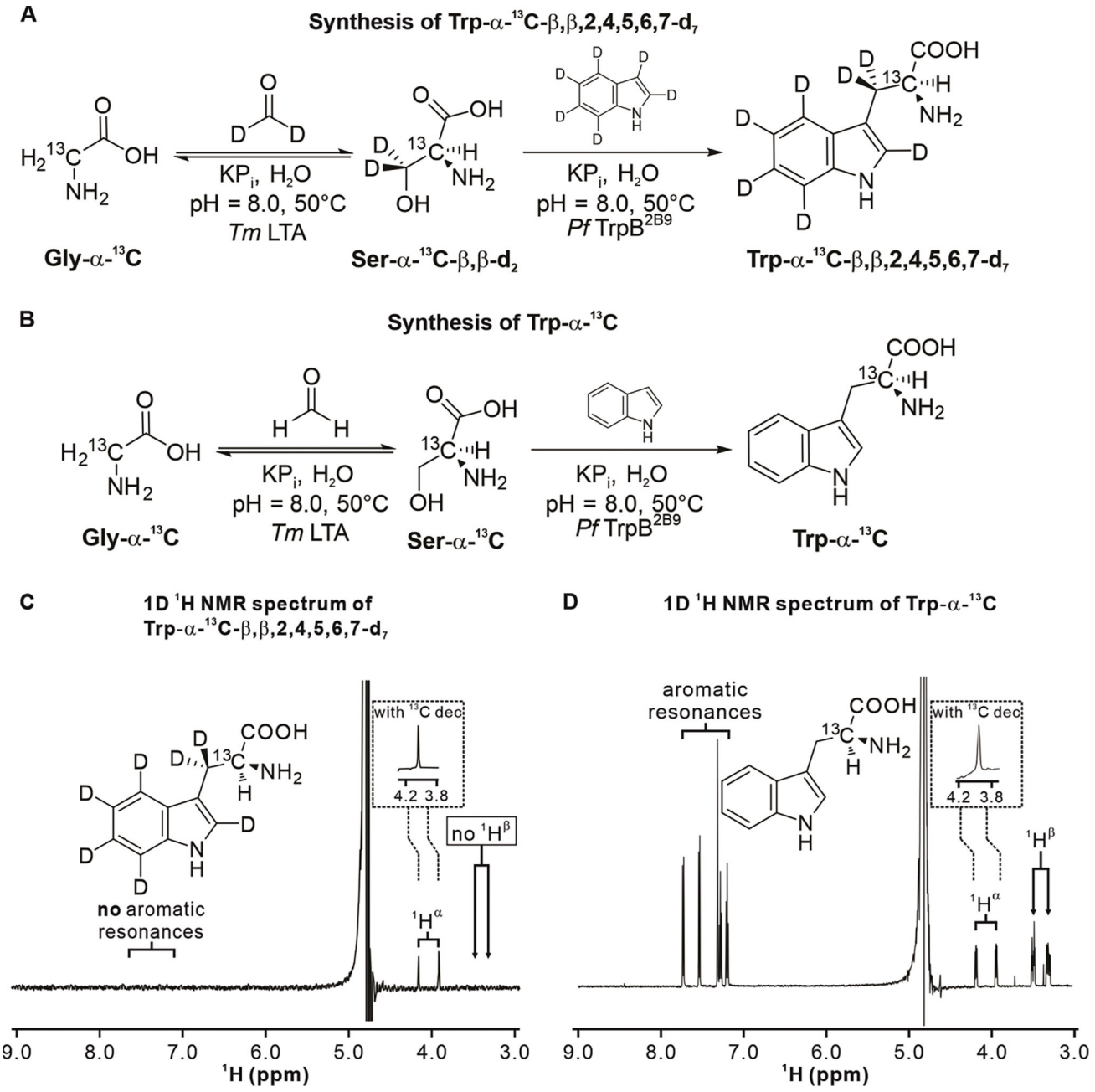

Figure 3. Synthesis and characterization of Trp isotopologs.

A. Scheme illustrating the enzyme-cascade synthesis of Trp-α-^{13}C-β,β,2,4,5,6,7-d$_7$. B. Scheme illustrating the enzyme-cascade synthesis of Trp-α-^{13}C. C. 1D ^{1}H NMR characterization of Trp-α-^{13}C-β,β,2,4,5,6,7-d$_7$. A pulse-acquire data-collection scheme with a 121.5 Hz solvent presaturation scheme during the entire 5 s recycle delay was employed. 8 scans were acquired. The sample (ca. 100 μM) was prepared in 90% H2O, 10% D2O with traces of sodium trimethylsilylpropanesulfonate (DSS) used as an internal reference. The inset shows the ^{1}H^α region of a spectrum including ^{13}C decoupling during acquisition using bi_p5m4sp_4sp.2 composite pulse decoupling (see Exp. Section in Suppl. Inf.). D. 1D ^{1}H NMR characterization of HPLC-purified and lyophilized Trp-α-^{13}C (ca. 200 μM). The inset

shows the $^{1}H^{\alpha}$ region of the ^{13}C-decoupled spectrum. The same acquisition and processing parameters as in panel C were used.

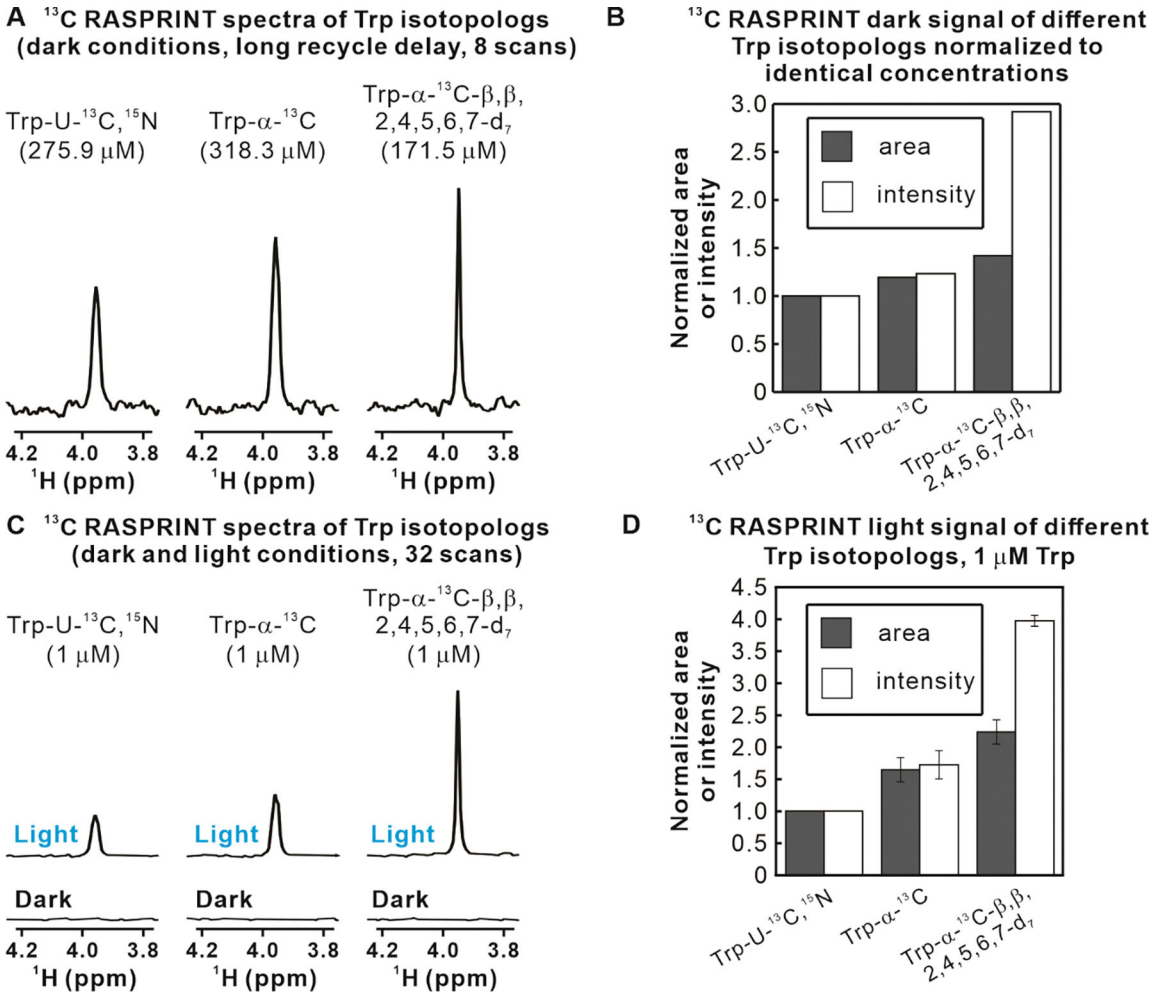

Figure 4. LED-off and LED-on data show enhancements due to both dark and light contributions.

A. NMR spectra showing the H^{α} resonance of different Trp isotopologs. Data were collected with the 1D ^{13}C RASPRINT pulse sequence under dark (i.e., LED-off) conditions at the concentrations listed above the spectra. A 5 s recycle delay was employed. B. Quantitative analysis of H^{α}-resonance areas and intensities-at-the-maximum relative to Trp-U-^{13}C,^{15}N, after normalization to eliminate differences due to variable concentrations. C. LC-photo-CIDNP spectra acquired with the 1D ^{13}C RASPRINT pulse sequence under light (LED-on) conditions for three Trp isotopologs of equal concentration. D. Quantitative analysis of H^{α} resonance area and intensity-at-the-maximum under light (i.e., LED-on) conditions relative to Trp-U-^{13}C,^{15}N. Data in panels B and D are shown as avg ± S.E. (n=2). All spectra were acquired at 24 °C with 64 scans, 4 dummy scans, and an optical irradiation time of 0.2 s.

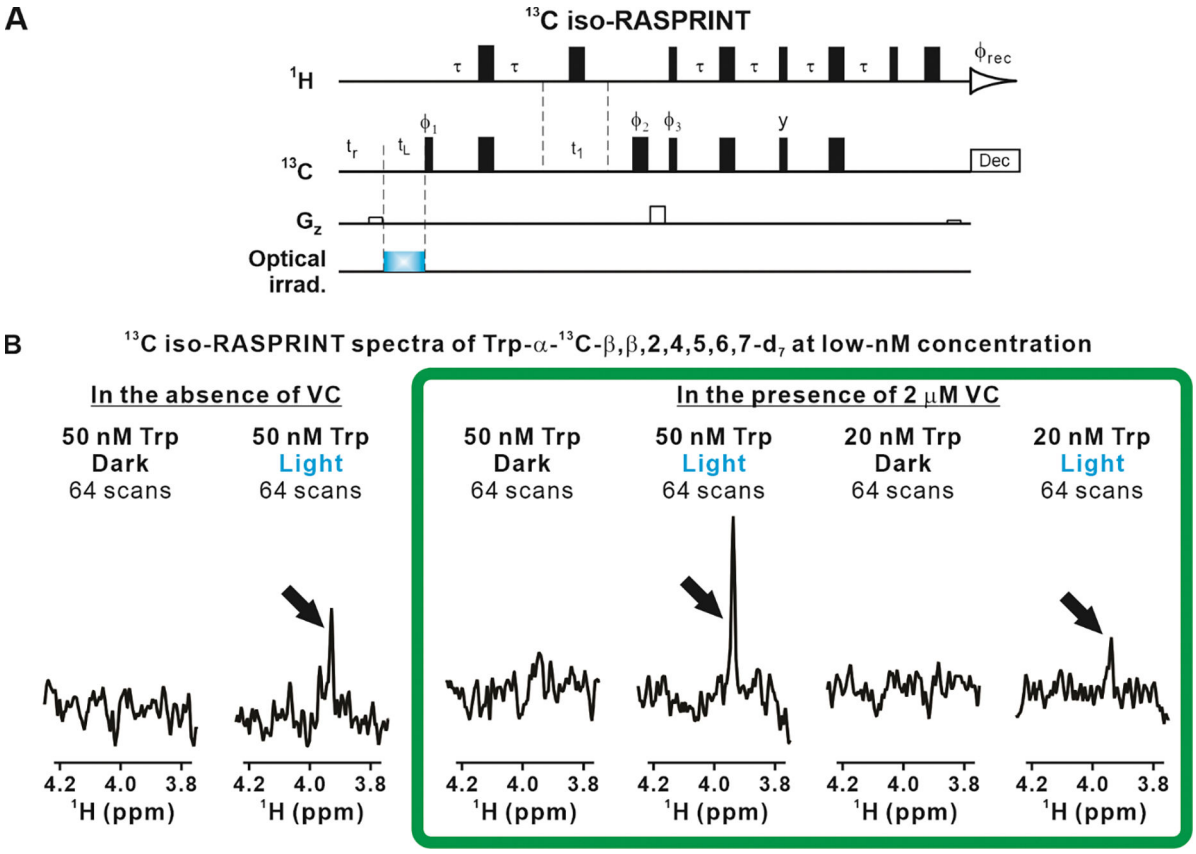

Figure 5. LC-photo-CIDNP in combination with selective isotope labeling enables the detection of Trp at low-nanomolar concentration.

A. Scheme illustrating the ^{13}C iso-RASPRINT pulse sequence, optimized for the detection of the Trp-α-^{13}C-β,β,2,4,5,6,7-d_7 isotopolog. The ^{13}C iso-RASPRINT sequence differs from the ^{13}C RASPRINT sequence in that on-resonance selective pulses are replaced by hard pulses and off-resonance selective pulses are removed. In addition, the constant-time evolution was removed, yet a short spin-echo was preserved to compensate for the effect of pulse field gradients. B. LC-photo-CIDNP (1D ^{13}C iso-RASPRINT) spectra of 50 and 20 nM Trp-α-^{13}C-β,β,2,4,5,6,7-d_7. Data were acquired under dark and light conditions, in the absence and presence of 2 μM vitamin C (VC). In each spectrum, signal-averaging was carried out across 64-scans preceded by 4 dummy scans. The optical irradiation time was 0.2 s. Data were collected at 24 °C. The spectra enclosed within the green frame show the highest degree of nuclear-spin hyperpolarization.

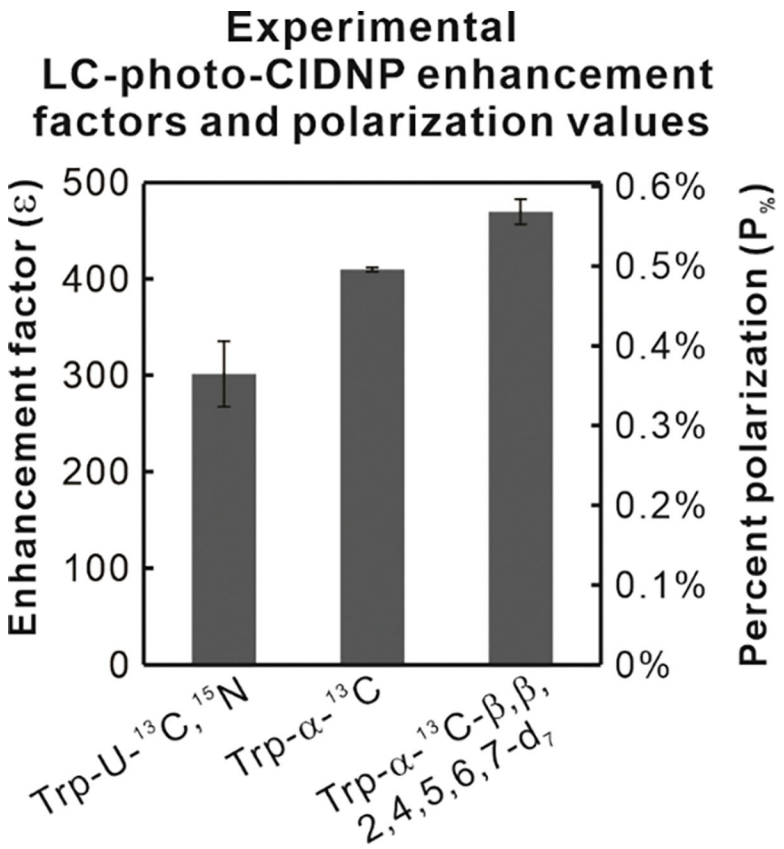

Figure 6. The Trp-α-^{13}C-β,β,2,4,5,6,7-d$_7$ isotopolog displays unprecedented LC-photo-CIDNP enhancement factors ε and percent polarization in solution.

Enhancement factors (ε) were determined from experimental data according to equation [3]. Percent polarization values were assessed from enhancement factors and thermal-equilibrium percent polarizations according to equation [4]. Thermal-equilibrium percent polarizations were estimated at room temperature at 600 MHz applied field. Sample concentrations were 1 μM and 100 μM in LED-on and LED-off experiments, respectively. All values are shown as avg ± S.E., with n=2, where n denotes the number of independent experiments.

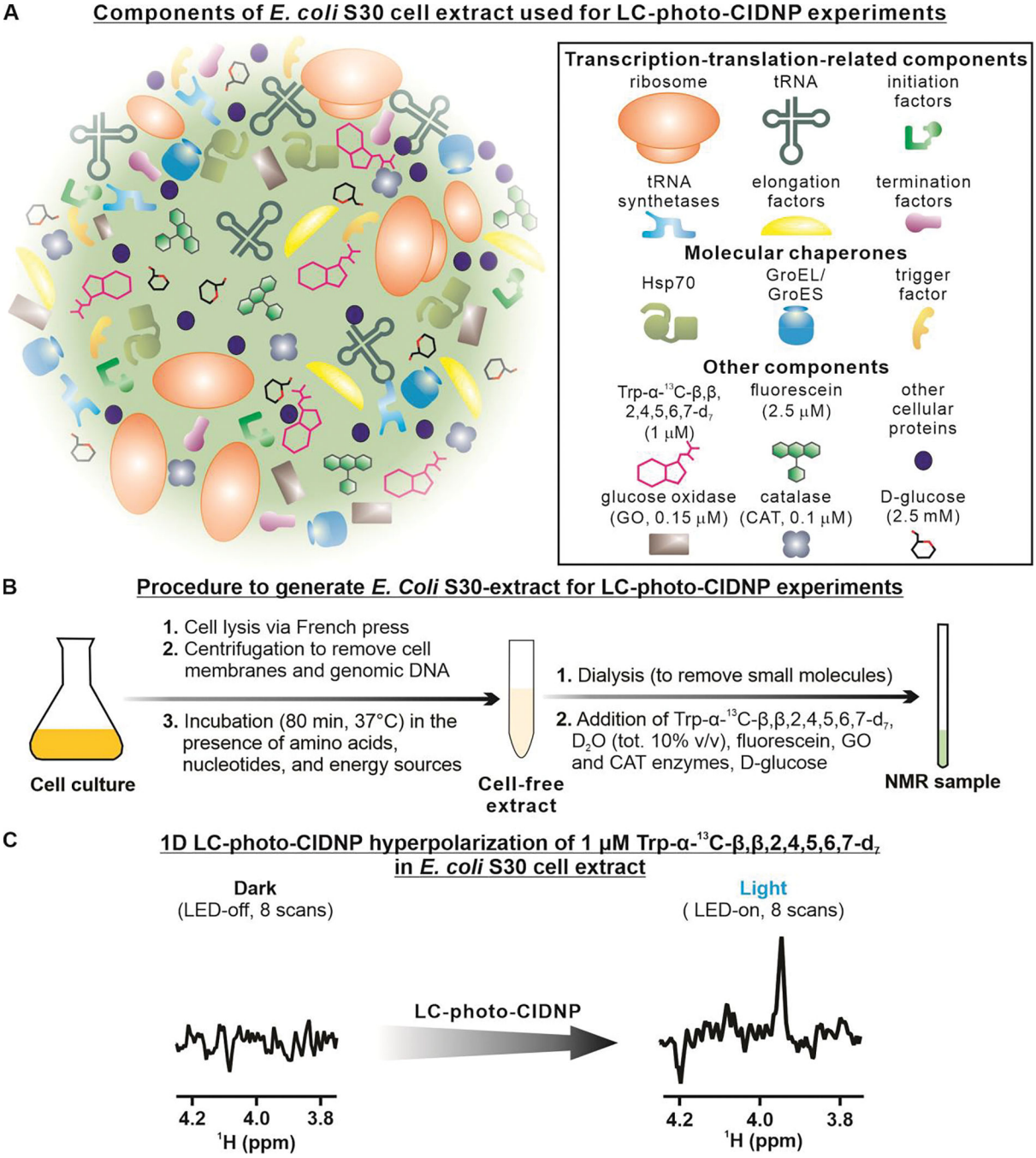

Figure 7. LC-photo-CIDNP in combination with selective isotope labeling enables hypersensitive data collection in a complex cell-like medium.

A. Schematic illustration of the components of the bacterial cell-like medium, i.e., an *E. Coli* S30 extract, employed in this work. B. Summary of the adopted procedures to generate the *E. Coli* S30 extract. C. LC-photo-CIDNP spectrum of 1 μM Trp-α-^{13}C-β,β,2,4,5,6,7-d7 in an *E. coli* S30 cell extract under dark (i.e., LED-off) and light (i.e., LED-on) conditions. Each spectrum was acquired at 24 °C with 8 scans, 4 dummy scans, and 0.2 s of optical irradiation.

Table 1.

Relative sensitivity of LC-photo-CIDNP NMR experiments (1D ^{13}C RASPRINT pulse sequence) carried out on different Trp isotopologs. The role of individual light (LED-on) and dark (LED-off) contributions is listed. Uniformly labeled Trp (Trp- U-^{13}C,^{15}N) is regarded as reference compound.

topolog	Relative sensitivity partitioned into individual contributions			Product of individual contributions [d]	Overall relative sensitivity (assessed via ^{13}C RASPRINT, light cond.) [e]
	LC-photo-CIDNP hyperpolarization [a] (light effect)	Elimination of J-coupling [b] (dark effect)	Linewidth reduction [c] (dark effect)		
Trp-U-^{13}C,^{15}N	100%	100%	100%	100%	100%
Trp-α-^{13}C	138±4%	119%	126 ± 2%	207 ± 7%	172 ± 20%
Trp-α-^{13}C-β,β, 2,4,5,6,7-d7	157±4%	142%	190 ± 5%	424 ± 16%	397 ± 9%

[a] Determined from data in Fig. 6, including assessment of errors.

[b] Determined from data in Fig. 4B. Only one experiment was carried out.

[c] Assessed from T_2 experiments in Supplementary Fig. S2. Values are shown as avg ± S.E., with n=3, where n denotes the number of independent experiments.

[d] Errors were assessed by error propagation of the individual contributions.

[e] Three ^{13}C RASPRINT experiments were carried out for each isotopolog under LED-on conditions. Relative sensitivities were assessed from resonance intensities of experiments run with identical parameters, including number of scans and duration. Relative sensitivities are shown as avg ± S.E.